Simulation of Computed Radiography X-ray Imaging Chain Dedicated to Complex Shape Objects

Min Yao, Philippe Duvauchelle, Valérie Kaftandjian, Angéla Peterzol-Parmentier, Andreas Schumm

Simulation of Computed Radiography X-ray Imaging Chain Dedicated to Complex Shape Objects

Min YAO [1], Philippe DUVAUCHELLE [1], Valérie KAFTANDJIAN [1], Angéla PETERZOL-PARMENTIER [2], Andreas Schumm [3]

[1] Laboratoire Vibrations Acoustique (LVA), INSA de Lyon; Lyon, France
Phone: +33 (0)4 72 43 82 13, Fax: +33 (0)4 72 43 88 22; e-mail: min.yao@insa-lyon.fr, philippe.duvauchelle@insa-lyon.fr, valerie.kaftandjian@insa-lyon.fr
[2] AREVA NDE-Solutions; Chalon-sur-Saône, France; E-mail: angela.peterzol-parmentier@areva.com
[3] EDF F&D SINETICS; Clamart, France; E-mail: andreas.schumm@edf.fr

Abstract
Computed Radiography (CR) based on photostimulable imaging plate (IP) is increasingly used in the field of non-destructive testing. For the inspections of high attenuation specimens employing high energy sources, the CR performance is poor because of the response of the IP. Simulation is a very useful tool to predict experimental outcomes and determine the optimal operating conditions. We propose a hybrid simulation approach which combines the use of both deterministic and MC codes for simulating rapidly a complex geometry imaging set-up. This approach allows us to take into account the degradation effect introduced by X-ray scattering and fluorescence transport as well as the optical photon scattering taking place in IP during X-ray exposure and optical readout processes. The results of different simulation configurations are compared.
Keywords: Radiographic testing (RT), modeling and simulation, nuclear, Monte Carlo-Deterministic simulation, computed radiography

1. Introduction

Computed radiography (CR), as a digital replacement of the traditional film radiography, is increasingly used in the field of non-destructive testing. As CR uses equipment very similar to the film radiography [1], the users do not need to modify their existing exposure routine. Moreover, the digital detector used, imaging plate (IP), is flexible (can be bent) and re-useful [2]. It is therefore easy to implement and cost-efficient. On the other hand, CR also has its limitations which hold back the industry from completely replacing the traditional radiography with such a technique. Today's available commercial IPs are mostly based on the high Z phosphor, which makes IP energy-dependent: sensitive to low energy and nearly transparent to high energy [3]. To overcome this problem, metallic screens are recommended, by current international standards [4], [5], to be used together with IP to ensure a good image quality. However, the type and thickness of such a screen are not clearly defined and a large panel of possible configurations does exist.

Simulation is a very useful tool to predict experimental outcomes and determine the optimal operating conditions. It makes it possible to study how the relevant operating parameters affect the x-ray image without actually testing it in real life. In the previous works, Vedantham and Karellas have developed a complete (from X-ray exposure to digital readout) analytic CR model to analyze the propagation of system performance factor, such as detective quantum efficiency (DQE) and modulation transfer function (MTF), during image formation process [6]. In their approach, the X-ray scattering effect is considered negligible. However, for high energy CR, where the scattering effect becomes dominant, this assumption is no longer appropriate. Souza et al. have proposed a methodology of computed radiography simulation for industrial applications [7], [8]. The IP dose response has been obtained using Monte Carlo method; scattering effect has been accounted. Whereas, the unsharpness introduced by energy deposition process has not been integrated, neither does the effect of metallic screen.

We propose a hybrid simulation approach which combines the use of both deterministic and MC codes. This approach allows us to simulate rapidly a complex geometry set-up and still take into account the physical phenomena (e.g. effect of metallic screens and x-ray or light scattering) during energy deposition and optical readout process. The results of different simulation configurations are compared.

2. Simulation method

In CR, the imaging plate is used to detect the transmitted radiation emerging from the object. The received radiation interacts with imaging plate resulting in a latent image, which is later read by an optical scanner. Accordingly, the simulation of the CR imaging chain follows three successive stages (Figure 1):

i. X- or gamma rays attenuation by object. At this stage, both Monte Carlo and deterministic methods can be used.

ii. Latent image generation. This stage consists of two steps: a) interaction of radiation with detector (IP alone or IP with screens); and b) latent image generation. For the former, the detector (IP alone or IP with screens) is modeled by a transfer function which is obtained through a parametric study using Monte Carlo simulation. The latter is simply modeled by an amplification factor, as the latent imaging forming mechanism is still not clearly understood, and furthermore, depending on the materials, the mechanisms are different.

iii. Digital image generation. There are also two steps in this stage: optical readout, and the collection, amplification and digitization of the emitted signal (i.e. photo-stimulated luminescence, PSL). The former is modeled by a transfer function (obtained with a Monte Carlo code) of the IP optical response; the latter is simply modeled as a factor without further blurring the output image.

Different simulation methods have been applied to the three stages, and will be discussed in sections 2.1, 2.2 and 2.3.

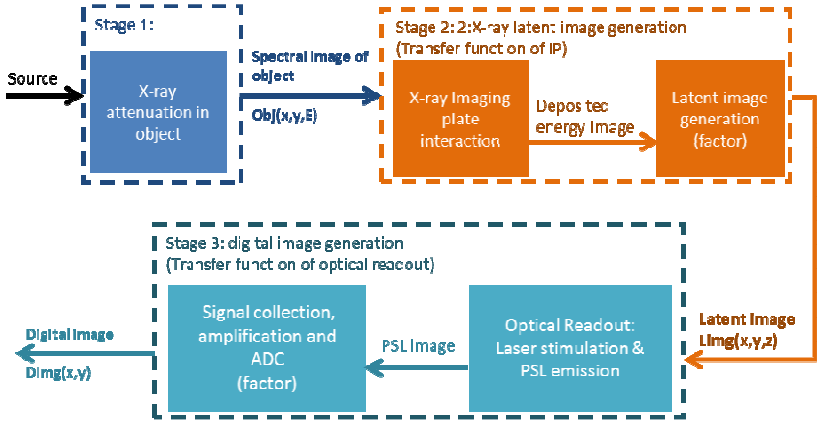

Figure 1: Computed radiography modeling. The CR imaging chain is modeled as three successive stages: x-ray attenuation by an object, latent image generation in IP and optical readout. The output of the previous stage is the input of the current stage. Certain sub-steps are treated as an amplification factor.

2.1 Generating object image

This stage simulates the interaction of radiation with object, and outputs an object image obj(*E, x, y*). Different methods (Monte Carlo or deterministic) could be employed depending on needs. To simulate a simple object, the Monte Carlo methods can deal with very detailed physical phenomena and provide precise results. However, modeling of complex objects with MC method is very time consuming; it would take months or even more. Moreover the manual design of complex geometry is quite frustrating and error-prone. In this case, deterministic methods can simulate rapidly complex set-ups under reasonable approximations; coupling with Computer Aided Design (CAD), the geometry designing can be relatively easy and robust.

In order to generate *obj*(*E, x, y*) (whichever method is chosen), a virtual detector is used and should be placed at the actual detector plane (see the green plane in Figure 2 (a)). This virtual detector is divided into M×N pixels to record the spatial distribution of the incident photons. Each pixel patch is also a spectrum counter with a channel width of E_{width} keV. In this way, the transmitted radiation is stored (Figure 2 (b)). The object image is in unit of photon number per pixel area per energy channel.

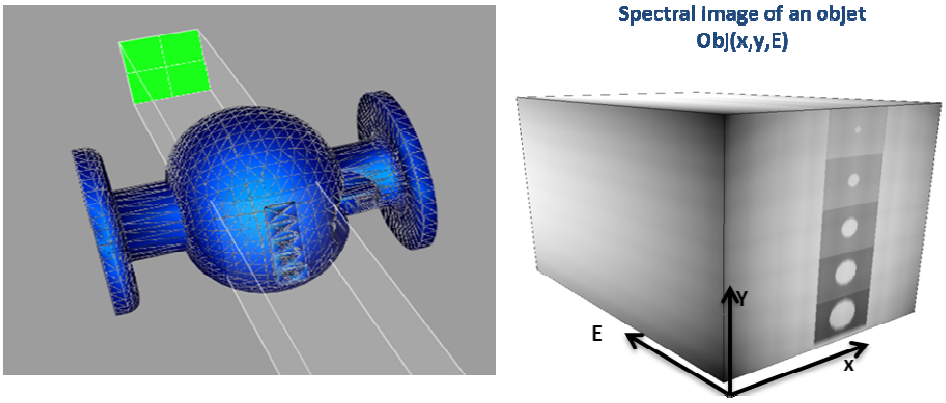

(a) (b)

Figure 2: Generation of the object image with a deterministic simulation tool VXI[9], [10]: (a) geometrical representation of imaging setup and (b) illustration of an output object image.

2.2 Generating latent image: CR detector model

The interaction of X-ray with detector is modeled by a transfer function H1 (Figure 3 (a)), which requires an object image *obj*(*E, x, y*) and a detector model $R_{x\text{-}ray}(det,E,x,y,z)$ as inputs. The object image is the output of the previous stage. The detector model is obtained through a parametric study of the CR detector. A Monte Carlo simulation tool, based on the use of PENELOPE, has been developed to characterize the CR detector response at different energies. The tool tracks separately the primary/secondary and photon/electron signals. It outputs 3D deposited energy maps due to different signals (see example in Figure 3(b)).

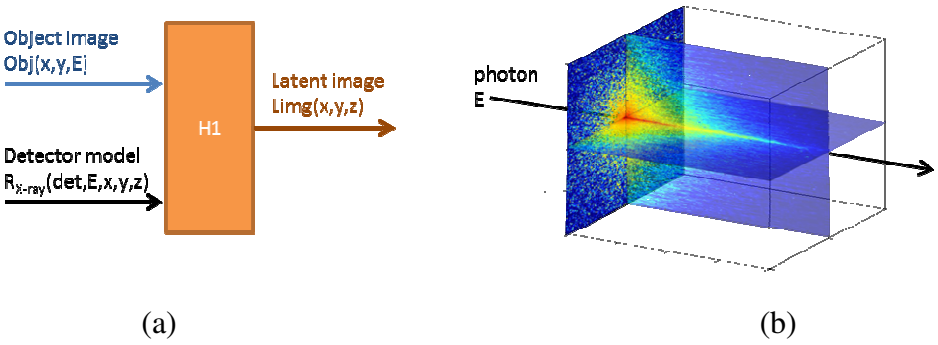

Figure 3: Latent image generation: (a) detector transfer function H1; and b) impulse response of detector (3D map of energy deposition).

We generate a set of impulse responses by varying the detector configuration *det* (i.e. IP/screens combination) and the incident energy *E*. With $R_{x\text{-}ray}(det,E,x,y,z)$, we can have the spectral response (Figure 4 (a)) by summing it over *x*, *y* and *z*; we can also calculate the spatial response (via the Fourier transform of the impulse responses) for different energies (Figure 4 (b)). The latent image is obtained through a convolution (H1) of the object image with the detector model

$$\begin{aligned} Limg(x,y,z) &= \mathrm{H1}(obj, R_{x-ray}) \\ &= \int_E \left(obj(E,x,y) * R_{x-ray}(\det_0, E, x, y, z) \right) dE \\ &= \int_E \left(\iint_{u,v} obj(E,x,y) \cdot R_{x-ray}(\det_0, E, x-u, y-v, z) du dv \right) dE, \end{aligned} \tag{1}$$

where *Limg(x,y,z)* is the latent image and $\det_0$ is the given detector.

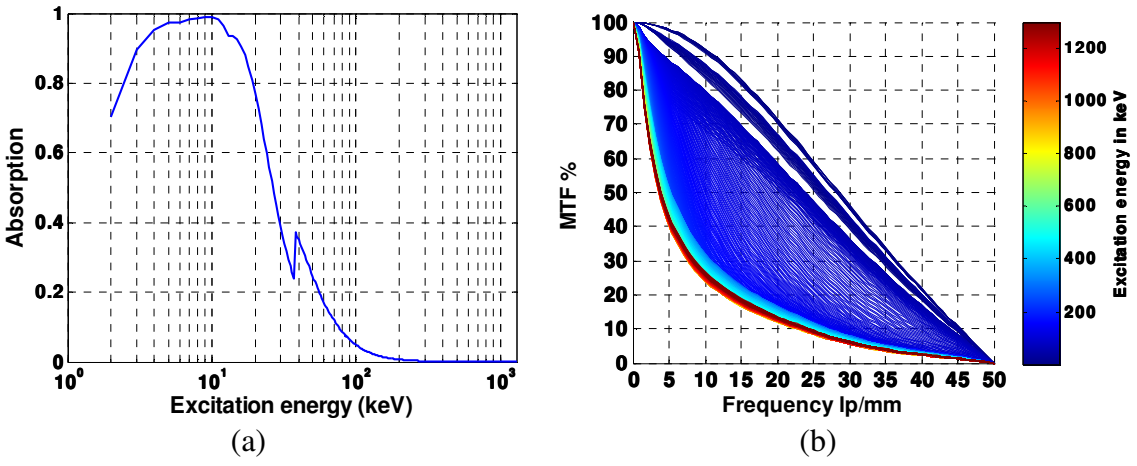

Figure 4: Spectral and spatial responses of IP (obtained with $R_{x\text{-}ray}(det,E,x,y,z)$).

2.3 Generating digital image: optical readout model

The optical readout process is viewed as a transfer function H2 (Figure 5 (a)), which also requires two inputs: latent image and IP model. Flying spot scanner is the most common CR

reader: a finely focused laser is used to scan and release, line by line, the latent image; the latent image is modified while the laser spot traverses the IP [11]. Thus different from the previous operator H1, H2 is a modified convolution operation. The final digital image is computed using

$$\begin{aligned} Dimg(x_0, y_0) &= \mathrm{H2}(Limg, I) \\ &= \int_z P(z)dz \iint_{x,y} Limg(x, y, z)\{1 - \exp[-\sigma \cdot I(x - x_0, y - y_0, z) \cdot t_{scan}]\}dxdy, \end{aligned} \tag{2}$$

where $Limg(x,y,z)$ is the latent image, $I(x,y,z)$ is the IP model (impulse response to a laser beam), $P(z)$ is the probability that a photon (emitted at z) could escape from the front side of IP, σ is the optical cross section of photo-stimulation and t_{scan} is the dwell time of laser spot at (x_0,y_0).

The IP model $I(x,y,z)$ is obtained through the Monte Carlo method. A Monte Carlo code has been programmed in Matlab to simulate the light propagation problem in IP. Certain physical models of light/IP interaction adopted in the code are based on [12] and [13]. Figure 5(b) shows us an example of IP response to a normal incident laser beam, to obtain which 2×10^6 photons has been generated to strike the imagine plate.

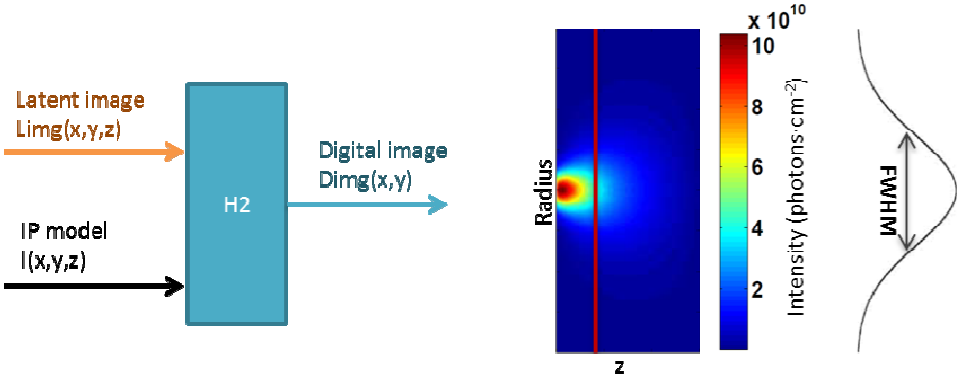

(a) (b)

Figure 5: a) Generation of the digital image using the optical readout transfer function H2; b) an example of IP model (impulse response of IP to laser light).

3. Results

The geometric set-up in Figure 2 has been adopted for our simulation. The object material was set steel, and it was irradiated by a monoenergetic point source (100 keV). A step/hole type image quality indicator (IQI) was placed on the object facing the source. Note that only the central part (where IQI located) has been exposed.

The detector was a combination of IP with metallic screens, where IP was sandwiched between the screens. The IP was modeled as a multi-layered structure which consists of, in sequence, a 6 μm protective layer, a 150 μm phosphor layer, a 254 μm support layer and a 25.4 μm backing layer. The materials of these four layers were respectively Mylar for the protective and support layers, $BaFBr:Eu^{2+}$ with a packing factor of 60% for the phosphor

layer, and polycarbonate for the backing layer. We have simulated the dose response of the following two detector configurations: a) IP alone ('HRIP') and b) IP with two 0.3 mm lead screens on both sides (0.3Pb+HRIP+0.3Pb).

3.1 Latent image

As a first step, we have computed the latent images generated by the two different detectors (see the upper two images in
Figure 6). In order to compare the contrast, the two images have been normalized by their maximum gray values. We plot the normalized profiles along the red lines below. In the image, the detector efficiency is also presented, denoted 'AE' (total energy absorbed in the phosphor layer over the total incident energy). With HRIP, about 4.92% of the object image has been detected. With lead screens, the efficiency decreases to 1.96% and we lose the contrast.

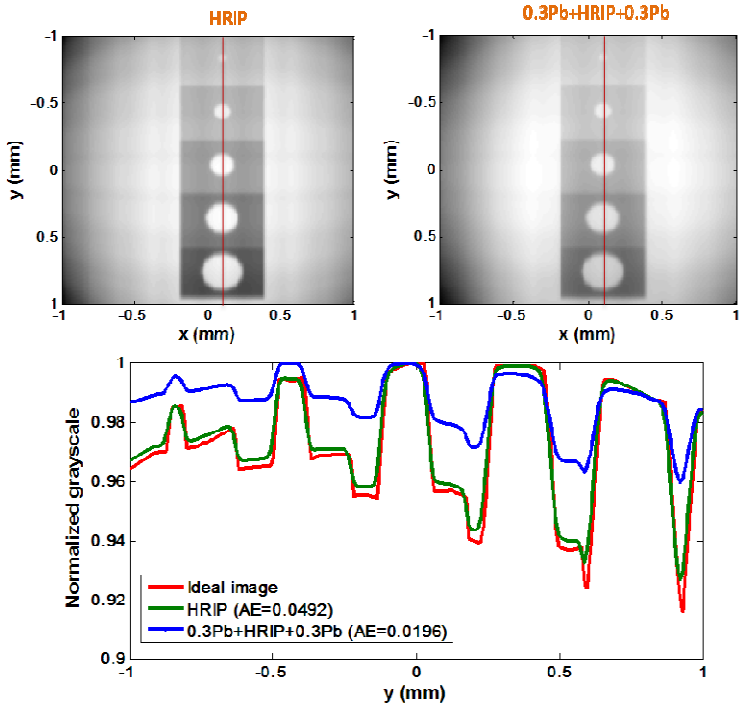

Figure 6: Simulation results: the latent images obtained with two different detector configurations.

3.2 Final output of simulation: digital image

In this part, the latent image generated with HRIP has been chosen as input. It has been read using different laser powers (represented by a power factor): 10^{10}, 10^{13}, 10^{14}, 10^{15} and 10^{16}. This factor is directly proportional to the laser power.

Figure 7 compares the object image, the latent image and two final images read with two different laser powers 10^{16} and 10^{10}. We lose the signal (gray level) and contrast after passing each stage. A great laser power leads a high gray level of the output image; however a slight shift upwards is observed (comparing
Figure 7 (c) with (b)). In the image obtained with '10^{16}', it is hard to identify the smallest hole.

We then plot reading efficiency (output signal over input signal) versus the laser power (

Figure 8). The efficiency increases slowly at low laser powers, then we see a significant increase between 10^{13} and 10^{15}; and at 10^{16} the curve starts to reach its maximum. One may notice that the maximum efficiency does not equal to one. Indeed, a high power increases the photoluminescence, but the photons are emitted isotropically and only a small fraction can escape from the front surface of IP and contribute to the final image.

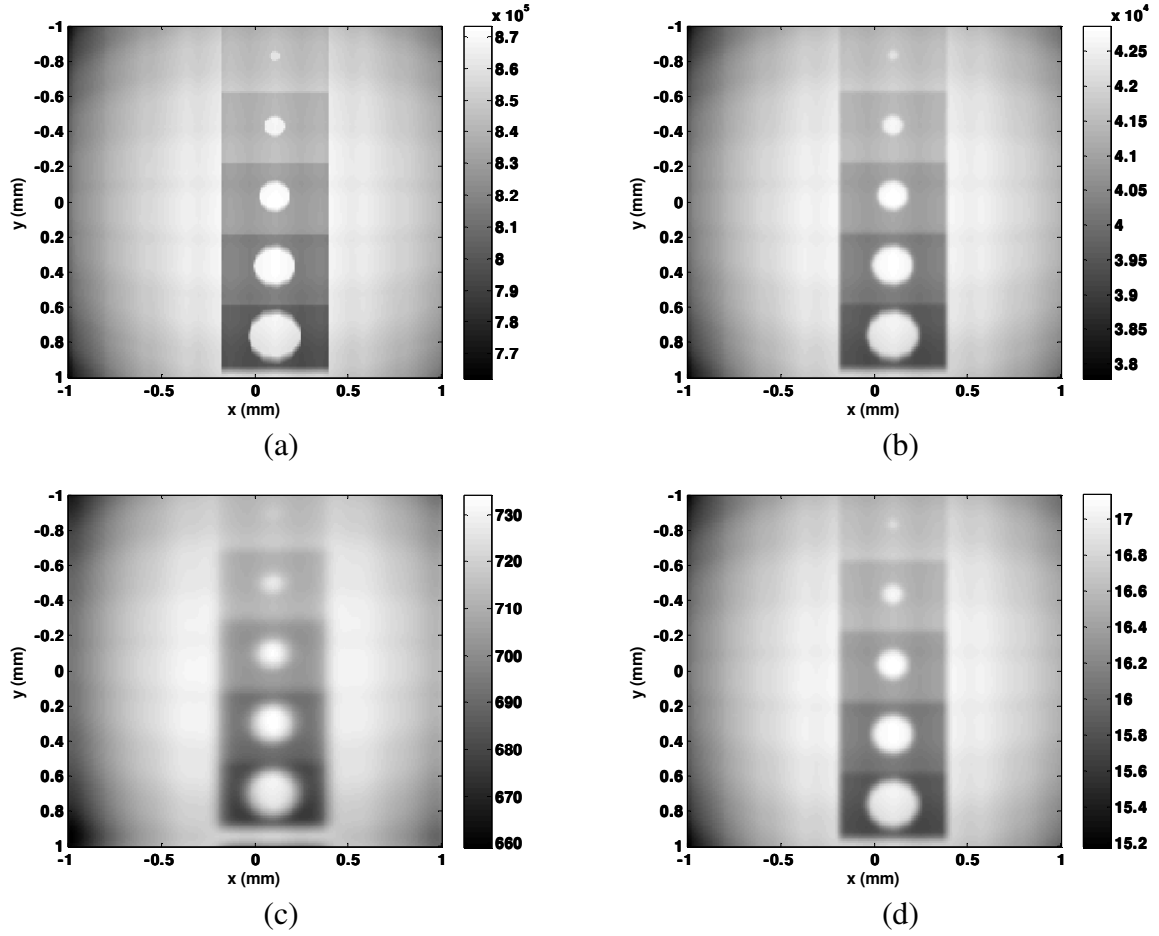

Figure 7: Simulation results: (a) object image, (b) latent image obtained with HRIP, (c) digital image output (reading factor 10^{16}) et (d) digital image (reading factor 10^{10}).

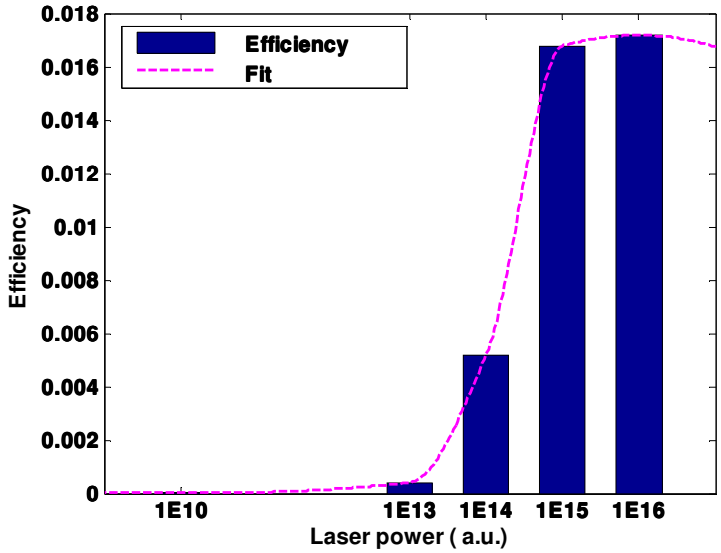

Figure 8: Readout efficiency versus laser power.

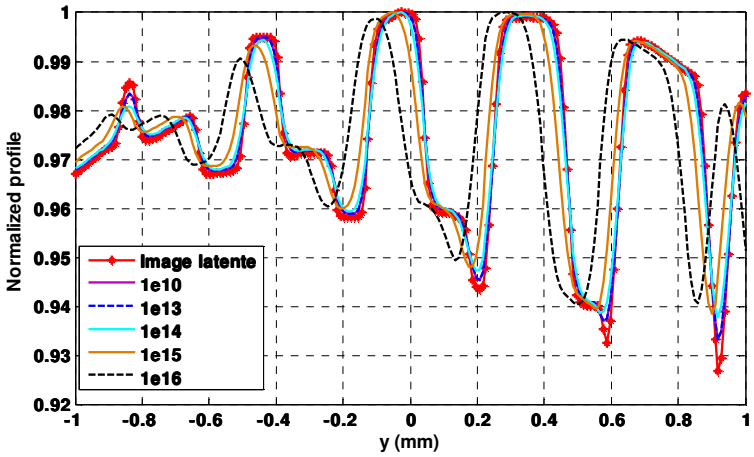

Figure 9: Normalized profiles for different laser power.

In order to compare the image contraste, the images have been nomalized by their maximum values. In Figure 9, we present the profiles along the IQI. The red curve is the latent image profile. The curves of the first 2 powers overlap each other, then we lose contrast by increasing the power. Comparing the profiles, we also see an obvious shift between the black and the red curves in the IP translation direction.

Finally, we show the evaluation of the profile after passing different stages in Figure 10. In this example, we took the optimal conditions for each stage: to detect the latent image with HRIP then read it with a laser power of '10^{15}'. We lose contrast at each stage.

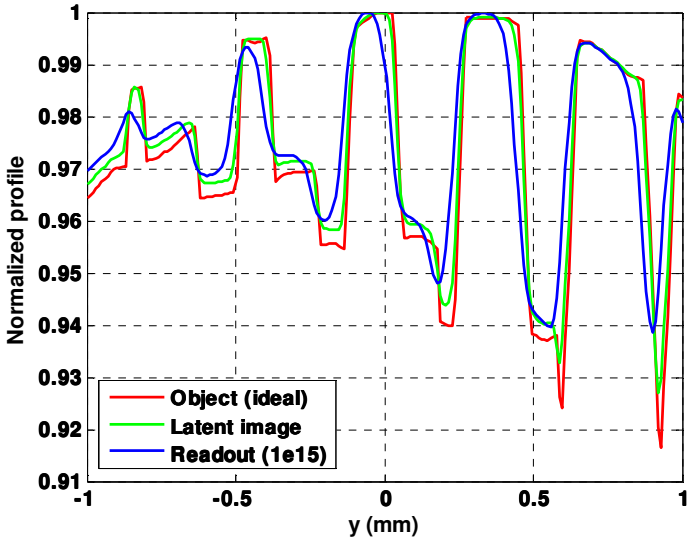

Figure 10: The object profile propagation. The red line is the object profile before entering the detector; the green line is the latent image detected by 'HRIP'; and the blue line is the output digital image read by the laser power '10^{15}'.

4. Discussion

In our case study, we have compared the image quality of different detection configurations (i.e. detector and laser power). The optimal imaging condition is obtained by using HRIP alone to receive the object image and reading the latent image with the laser power '10^{15}'.

For the optical readout, with the increase of the laser power, the reading efficiency increases (i.e. the fraction of the electrons released by the laser); however we loss the contrast. The reason is that when reading the current point, part of the trapped electrons in the neighborhood are also released and contribute to the signal of the current pixel resulting in blurring. The more we increase the laser power, the more the surrounding pixels are affected. This is also the reason that we observe a shift while using a very high laser power. To optimize the efficiency and to optimize the contrast are two conflicting goals. Compromises should be made for different applications.

5. Conclusion

We have presented an approach to simulating the computed radiography imaging chain. Different simulation methods have been adopted: the Monte Carlo and deterministic methods. A simulation tool has been developed based on this approach. We have showed the use of our tool via a case study. With the tool we can simulate the influence of different parameters such as detector configuration and laser power. One can use it to study the CR system performance, and optimize the image quality.

The comparison between simulation and experimental results is in progress.

References

1. M. Sonoda, M. Takano, J. Miyahara, and H. Kato, 'Computed radiography utilizing scanning laser stimulated luminescence', Radiology, Vol. 148, No. 3, pp. 833–838, Sep. 1983.
2. H. von Seggern, 'Photostimulable x-ray storage phosphors: a review of present understanding', Braz. J. Phys., Vol. 29, No. 2, pp. 254–268, 1999.
3. J. A. Rowlands, 'The physics of computed radiography', Phys. Med. Biol., Vol. 47, No. 23, p. R123, 2002.
4. 'Non-destructive testing - Industrial computed radiography with storage phosphor imaging plates - Part 2: General principles for testing of metallic materials using X-rays and gamma rays', EN 14784-2, 2005.
5. 'Non-destructive testing of welds -- Radiographic testing -- Part 2: X- and gamma-ray techniques with digital detectors', ISO 17636-2, 2009.
6. S. Vedantham and A. Karellas, 'Modeling the performance characteristics of computed radiography (CR) systems', IEEE Trans. Med. Imaging, Vol. 29, No. 3, pp. 790–806, Mar. 2010.
7. E. M. Souza, S. C. A. Correa, A. X. Silva, R. T. Lopes, and D. F. Oliveira, 'Methodology for digital radiography simulation using the Monte Carlo code MCNPX for industrial applications', Appl. Radiat. Isot. Data Instrum. Methods Use Agric. Ind. Med., Vol. 66, No. 5, pp. 587–592, May 2008.
8. S. C. A. Correa, E. M. Souza, A. X. Silva, D. H. Cassiano, and R. T. Lopes, 'Computed radiography simulation using the Monte Carlo code MCNPX', Appl. Radiat. Isot., Vol. 68, No. 9, pp. 1662–1670, Sep. 2010.
9. P. Duvauchelle, N. Freud, V. Kaftandjian, and D. Babot, 'A computer code to simulate X-ray imaging techniques', Nucl. Instruments Methods Phys. Res. Sect. B Beam Interactions Mater. Atoms, Vol. 170, No. 1, pp. 245–258, 2000.
10. N. Freud, P. Duvauchelle, S. A. Pistrui-Maximean, J.-M. Létang, and D. Babot, 'Deterministic simulation of first-order scattering in virtual X-ray imaging', Nucl. Instruments Methods Phys. Res. Sect. B Beam Interactions Mater. Atoms, Vol. 222, No. 1–2, pp. 285–300, Jul. 2004.
11. P. Leblans, D. Vandenbroucke, and P. Willems, 'Storage phosphors for medical imaging', Materials, Vol. 4, No. 6, pp. 1034–1086, 2011.
12. L. Wang, S. L. Jacques, and L. Zheng, 'MCML—Monte Carlo modeling of light transport in multi-layered tissues', Comput. Methods Programs Biomed., Vol. 47, No. 2, pp. 131–146, 1995.
13. R. Fasbender, H. Li, and A. Winnacker, 'Monte Carlo modeling of storage phosphor plate readouts', Nucl. Instruments Methods Phys. Res. Sect. Accel. Spectrometers Detect. Assoc. Equip., Vol. 512, No. 3, pp. 610–618, Oct. 2003.